

# Pancharatnam–Berry optical elements for head-up and near-eye displays [Invited]

TAO ZHAN,<sup>1</sup> YUN-HAN LEE,<sup>1</sup> GUANJUN TAN,<sup>1</sup> JIANGHAO XIONG,<sup>1</sup> KUN YIN,<sup>1</sup> FANGWANG GOU,<sup>1</sup>  JUNYU ZOU,<sup>1</sup> NANNAN ZHANG,<sup>2</sup> DONGFENG ZHAO,<sup>2</sup> JILIN YANG,<sup>2</sup> SHENG LIU,<sup>2</sup> AND SHIN-TSON WU<sup>1,\*</sup>

<sup>1</sup>CREOL, The College of Optics and Photonics, University of Central Florida, Orlando, Florida 32816, USA

<sup>2</sup>GoerTek Electronics, 5451 Great America Parkway, Suite 301, Santa Clara, California 95054, USA

\*Corresponding author: swu@creol.ucf.edu

Received 29 November 2018; revised 15 January 2019; accepted 19 January 2019; posted 24 January 2019 (Doc. ID 353161); published 22 February 2019

Liquid-crystal-based Pancharatnam–Berry phase optical elements (PBOEs), also known as diffractive wave plates (DWP), geometric phase optics (GPO), or geometric phase holograms (GPHs), are functional planar structures with patterned orientation of anisotropy axis. Several scientifically interesting yet practically useful electro-optical effects, such as focusing, beam splitting, waveguide coupling, and wavelength filtering, have been realized with PBOEs. Because of the high degree of optical tunability, polarization selectivity, nearly 100% diffraction efficiency, and simple fabrication process, PBOEs have found widespread applications in emerging display systems, particularly virtual/augmented/mixed reality displays and head-up displays. In this review, we will describe the basic operation principles, present device fabrication procedures, discuss numerical modeling methods, and address applications of PBOEs in emerging display systems. © 2019 Optical Society of America

<https://doi.org/10.1364/JOSAB.36.000D52>

## 1. INTRODUCTION

Unlike conventional refractive optics that utilize the optical path difference to produce phase patterns [1,2], liquid-crystal (LC)-based Pancharatnam–Berry phase optical elements (PBOEs) [3–7] generate the desired phase profile by spatially varying the LC directors. Because of their high diffraction efficiency [8,9], strong polarization dependency, and high optical quality, these promising functional planar optical elements have been implemented in several information display systems because of their distinct optical properties.

The working principle of PBOEs in the Raman–Nath region [10] can be easily illustrated by the Jones calculus:

$$J_{\pm} = \frac{1}{\sqrt{2}} \begin{bmatrix} 1 \\ \pm j \end{bmatrix}, \quad (1)$$

where  $J_{+}$  and  $J_{-}$  are the Jones vectors of left- and right-handed circularly polarized light (LCP and RCP). After being modulated by a half-wave plate oriented at angle  $\psi$ , the Jones vectors of output beam can be derived as

$$J'_{\pm} = R(-\psi)W(\pi)R(\psi)J_{\pm} = -je^{\pm 2j\psi}J_{\mp}, \quad (2)$$

where  $R(\psi)$  is the rotation matrix and  $W(\pi)$  is the half-wave retardation Jones matrix. The handedness of output light is switched, and a spatial-varying phase that is determined by the local azimuthal angle  $\psi$  is accumulated.

Various kinds of PBOEs have been demonstrated in recent years, including but not limited to gratings [11–18], lenses

[12,16,19–26], axicons [16,27], vortex wave plates [16,28–31], and other complex elements [27,32–37]. Apparently, PBOEs patterned with lens and deflector (grating) profiles, as shown in Fig. 1, are of more interest for display applications.

It should be emphasized that polarization handedness switches when the light passes through PBOEs, and the PBOEs manifest conjugate functions for the RCP and LCP light, because the accumulated phase profile has opposite signs for each handedness, as shown in Eq. (2). Thus, a Pancharatnam–Berry (PB) lens (PBL) with positive optical power  $K$  for LCP shows negative optical power  $-K$  for RCP. Also, a PB deflector (PBD) would also diffract RCP and LCP light to opposite directions, as illustrated in Fig. 2.

With their pronounced polarization dependency, two types of dynamic switching can be realized: active and passive. For passive switching, the PBOEs are not switched directly. Rather, we place an electrically switchable polarization rotator (e.g., a 90° twist-nematic LC cell with a  $\lambda/4$  plate) in front of the PBD or PBL. By controlling the polarization handedness of the incoming beam, the PBOE will function differently, as Fig. 2 depicts. On the contrary, for active switching, the PBOEs are usually made of indium tin oxide (ITO) glass substrates. By directly applying a voltage across the PBOE device, the LC directors will be reoriented from patterned half-wave plate to homeotropic state, as Fig. 3 depicts.

In a passive driving scheme, the switching element is on the polarization rotator, instead of the PBOE itself. As a result,

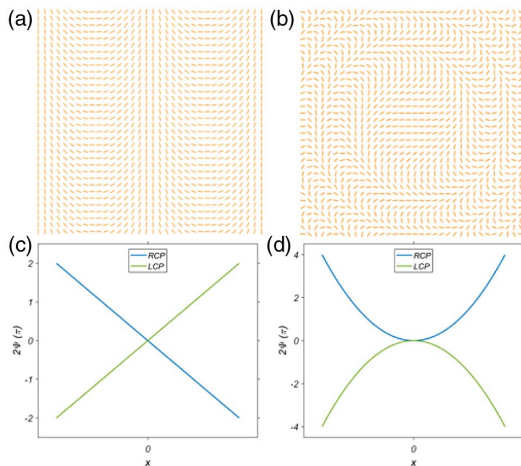


**Fig. 1.** Schematic distribution of LC anisotropy axis orientation in (a) a PB deflector and (b) a PB lens. The corresponding phase change of the (c) PBD and (d) PBL.

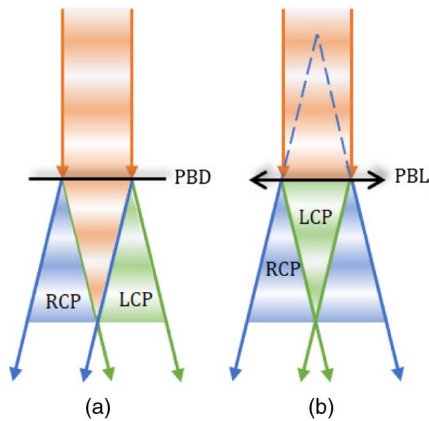


**Fig. 2.** Illustration of polarization dependency of PBOEs: (a) PBD diffracts RCP light to +1 order and LCP light to -1 order; (b) PBL serves as a diverging lens for input LCP light but a converging one for input RCP light.

both LC and LC-polymeric film can be considered for PBOEs. In practice, LC polymer is a common choice for passive driving because it offers more degrees of freedom to tailor the spectral and angular response of PBOEs for specific applications through twisted multi-layer structures in the axial (or  $z$ )

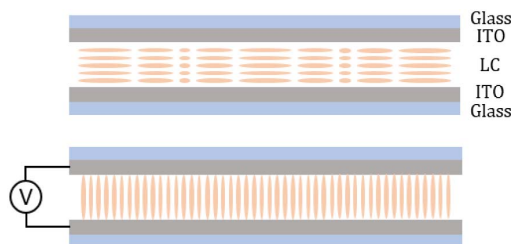


**Fig. 3.** Schematic illustration of PBOEs made of LCs sandwiched between transparent electrodes (upper) before and (lower) after dynamic switching.

**Table 1. Driving Method of PBDs and PBLs**

	w/o Voltage		w/Voltage	
	RCP	LCP	RCP	LCP
Input polarization	RCP	LCP	RCP	LCP
PBL optical power	$K$	$-K$	0	0
PBD diffraction order	1	-1	0	0
Output polarization	LCP	RCP	RCP	LCP

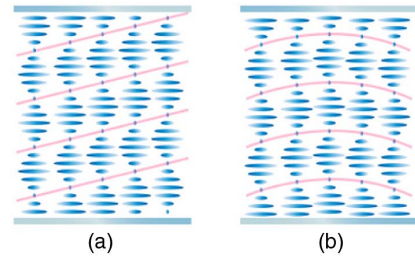


**Fig. 4.** Schematic presentation of the anisotropy axis orientation: (a) Bragg PBD, also referred as polarization volume grating (PVG) or Bragg polarization grating; (b) reflective PBL based on cholesteric liquid crystal (CLC).

direction (perpendicular to the substrates). On the other hand, for an active driving device, the switching burden falls on the PBOE itself. Thus, LC instead of LC polymer should be used [38]. Table 1 summarizes the driving schemes of PBDs and PBLs and their corresponding optical effects.

Recently, high-efficiency PBOEs in the Bragg region, usually with a high degree of twist in the axial direction, have been developed [12,14,17], and their anisotropy axis orientation patterns are illustrated in Fig. 4. The PBOEs in the Bragg region could be made both transmissive and reflective by engineering their twist structures. Also, a Bragg PBOE [15,39] generally provides large deflection angle and manifests higher spectral and angular selectivity than PBOEs in the Raman–Nath region.

## 2. DEVICE FABRICATION

### A. LC Alignment

Since PBOEs for display applications must manifest high optical quality without detrimental defects, the photoalignment method [40,41] is a favored choice over mechanical buffing [42] to pattern the LC molecules as linear or parabolic patterns for high-quality PBDs and PBLs, respectively. Two types of photoalignment methods, surface and bulk alignment, have been reported for fabricating PBOEs.

#### 1. Surface Alignment

Surface alignment is the most established method so far for PBOE fabrication, as shown in Figs. 5(a) and 5(b). Various types of photoalignment materials [43] can be employed to pattern the LC director using different mechanisms, such as cis–trans isomerization, dimerization, and non-chemical light-induced reorientation. The photoalignment materials should have strong azimuthal anchoring energy and manifest a high order parameter to ensure the quality of PBOEs. For the fabrication of electrically responsive PBOEs, first two ITO-glass

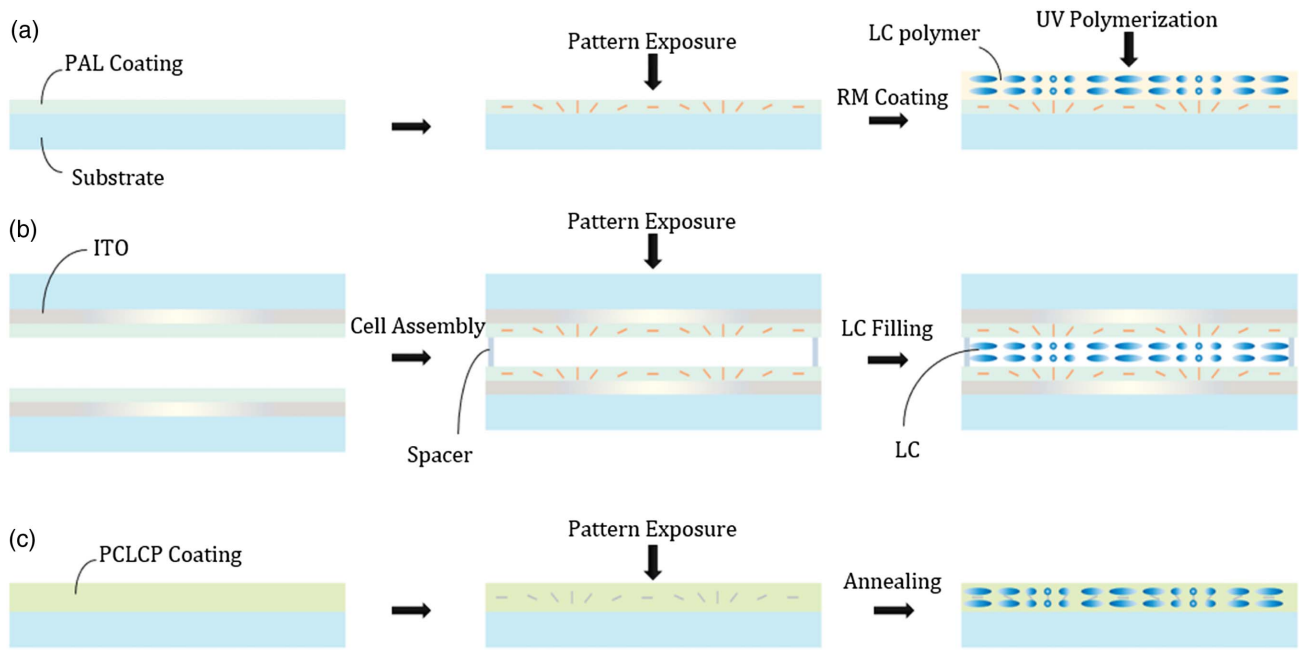


**Fig. 5.** Schematic illustration of fabrication procedures of PBOEs. Surface alignment for (a) LC polymer film PBOEs and (b) electrically responsive LC PBOEs. (c) Bulk alignment using a PCLCP film.

substrates coated with a photoalignment layer (PAL) [44–49] are assembled as a uniform LC cell, where the cell gap is controlled to match the half-wave retardation ( $\Delta nd = \lambda/2$ ) for achieving high efficiency at an intended wavelength. After undergoing photoalignment exposure, the cell is filled with LC via capillary action at a temperature above the clear point of the LC material [50]. The LC molecules are then aligned by surface anchoring from the PAL when cooling to room temperature. The diffraction efficiency of the fabricated switchable PBOEs can be modulated by applying a voltage [51] above the threshold of the LC cell.

To fabricate a polymer-film-based PBOE, we first coat or spray a thin PAL on the glass substrate surface and then expose it with a polarized light field to generate the desired patterns. Next, we spin-coat or spray the prepared LC reactive mesogen (RM) mixture (typically including LC monomers, solvents, photo-initiators [52,53], and surfactants [54]) onto the patterned surface [55] such that the LC molecules are aligned following the patterns of the photoalignment material or the previous RM layer. Finally, we expose the sample with ultraviolet light for polymerization.

## 2. Bulk Alignment

Recently, bulk alignment of Bragg PBDs [17] was realized by an all-in-one-material approach using a photo-crosslinkable LC polymer (PCLCP) and two-step material processing, as illustrated in Fig. 5(c). The PCLCP film containing mesogenic biphenyl side groups and photoreactive cinnamic ester side groups [56,57] is initially isotropic and transparent after being coated on a glass substrate. The exposure of the LC layer under a polarization light field at room temperature results in the photoselective cycloaddition of the cinnamic ester groups. Then, the bulk alignment of LC occurs when the film is annealed

above the glass transition temperature, significantly enhancing the anisotropy of the material [58].

## B. Polarization Field Generation

### 1. Interferometry Approach

Polarization interferometry is commonly utilized to generate a high-quality linearly polarized light field with patterned directions. Several types of interferometer could be adapted for the pattern exposure step in the fabrication process of PBDs and PBLs.

The conventional exposure setup [59,60] for PBDs is illustrated in Fig. 6(a). The linearly polarized laser beam is split evenly into two arms by the non-polarizing beam splitter (NPBS). After being deflected by the mirrors (M), the polarization states of the two beams are converted to orthogonally circular polarizations (RCP and LCP) by two quarter-wave plates (QWPs). Thus, a polarized light field with linearly changing orientation is generated on the substrate (S) for the fabrication of PBDs. This simple setup is suitable to fabricate PBDs with relatively small grating periods but not practical for PBDs with large ones, since when the angle between RCP and LCP beams is too acute the footprint of the whole setup could be enormous. Moreover, with the double-path configuration, this setup is highly sensitive to the relative phase and length changes in the two arms. As a result, the unobservable vibration of the optical table and airflow could significantly deteriorate the optical quality of PBDs fabricated with this setup.

Figure 6(b) shows a modified Sagnac interferometer designed by our group for PBOE pattern exposure. The polarization state of the linearly polarized input beam is rotated by a half-wave plate (HWP) to ensure that the RCP and LCP output

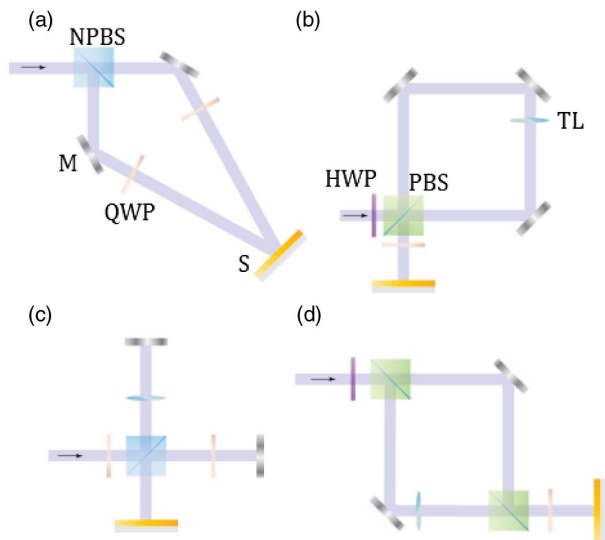


**Fig. 6.** Schematic illustration of polarized exposure pattern generation optical setups based on (a) two beam, (b) Sagnac, (c) Michelson, and (d) Mach-Zehnder interferometry. (NPBS, non-polarizing beam splitter; M, mirror; QWP, quarter-wave plate; S, substrate; HWP, half-wave plate; TL, template lens).

beams share the same intensity. The polarizing beam splitter (PBS) separates the  $s$ - and  $p$ -polarized components by reflecting the  $s$  polarization while allowing the  $p$  polarization to pass. The  $p$ -wave and  $s$ -wave propagate around four sides of the rectangle in the opposite direction and then combine at the original PBS. A QWP is placed at the output port to convert  $s$  and  $p$  polarization into RCP and LCP, such that a spatial-varying linear polarization pattern is generated on the substrate. For PBLs, a template lens (TL) or a set of TLs could be placed in the loop, providing a parabolic patterned linear polarization light field. It is worth mentioning that this interferometric approach is feasible for fabricating PBLs with an area much larger than the dimension of the optics used in the setup. For PBDs, the TL is removed and the PBD period can be controlled merely by tuning the orientation angle of the PBS or the second mirror. Considering the common-path nature of a Sagnac interferometer, this type of exposure setup is highly tolerant to environmental vibrations, which is a significant advantage over other configurations.

Moreover, there is another type of common-path exposure setup exploiting Wollaston prisms [61,62] to efficiently produce the linear pattern for fabricating PBDs, which may be considered a modified Fresnel's biprism interferometer.

Figures 6(c) and 6(d) demonstrate two similar exposure setups [20,63,64] modified from Michelson and Mach-Zehnder interferometers, respectively. The optical path of the exposure installation based on a Michelson interferometer could be considered a folded version of the Mach-Zehnder one. Both of them can be utilized for the fabrication of PBLs by placing a TL system in one arm and of PBDs by rotating the BS or mirrors. Because of their double-path nature, the whole setup should be placed on an optical table with a vibration isolation system and covered with optical enclosures to minimize environmental perturbations.

## 2. Non-Interferometry Approach

The polarized light field for fabricating PBOEs can also be generated without polarization interferometry. Digital polarization holography [55] utilizing a pixelated spatial light polarization converter can record arbitrary polarization distribution on a pixel-by-pixel level, as depicted in Fig. 7(a). The linearly polarized collimated laser beam is converted to circular polarization by a QWP and then reflected by a spatial light modulator with high pixel density. The modulated laser beam is changed back to linear polarization by the second QWP and imaged onto the substrate coated with the photoalignment material. Although the resolution of this method is limited by the pixel density of the SLM, this method provides a convenient one-shot solution for arbitrary PBOEs, including PBDs and PBLs.

A digital micromirror device (DMD)-based lithography system [33,65–67] with a rotatable polarizer can produce an arbitrary pattern for photoalignment, as shown in Fig. 7(b). A collimated UV beam reflected and modulated by a DMD is projected to the substrate for alignment. The reflected beam from the surface of the substrate is then collected by a charge-coupled device (CCD), assuring accurate focusing of the image. By synchronizing the pattern generated by the DMD and the orientation angle of the polarizer, exposure patterns for arbitrary PBOEs can be produced by this setup.

Another type of non-interferometry approach uses a motorized 1D polarization rotator (PR) and 1D/2D motion stage (MS) to direct write [16,27,28,68–70] a polarization pattern

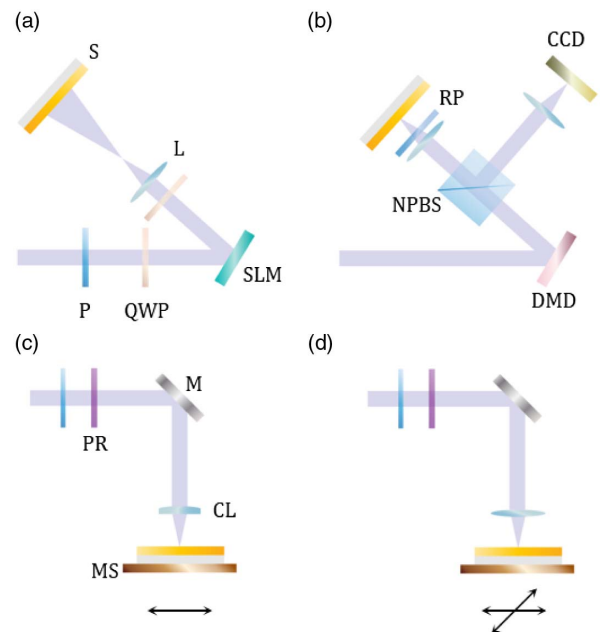


**Fig. 7.** Schematic illustration of optical setups for polarized exposure pattern generation, including (a) digital polarization holography enabled by a spatial light modulator, (b) DMD-based digital lithography and direct writing method with (c) 1D and (d) 2D spatial scanning. (P, polarizer; QWP, quarter-wave plate; SLM, spatial light modulator; L, lens; S, substrate; DMD, digital micromirror device; NPBS, non-polarizing beam splitter; RP, rotatable polarizer; CCD, charge-coupled device; PR, motorized polarization rotator; M, mirror; CL, cylindrical lens; MS, motorized motion stage).

through continuous scanning of a focused laser line/spot with the desired polarization angle, as shown in Figs. 7(c) and 7(d). This straightforward approach can also produce arbitrary phase patterns. It is worthwhile to mention that, thanks to the interaction between LC and PAL, this approach can generate features even smaller than the size of the focused scanning beam [16].

### 3. EMERGING DISPLAY APPLICATIONS

#### A. PB Deflector

##### 1. Pixel Density Enhancement

The limited pixel density and apparent screen-door effect of virtual reality (VR) displays [71,72] significantly degrade the desired immersive experience for viewers. The angular resolution of a 20/20 vision human visual system is around 1 arcmin, posting a hard target for VR displays with a large field of view (FOV > 110°). As an attempt to deal with this issue, a pixel density enhancement method for near-eye display was developed [73,74] based on a switchable PBD cell without changing the physical pixel density of the display panel. The PBD in the optical system functions as a non-mechanical pixel shifter to double the apparent pixel density, as illustrated in Fig. 8(a). The PBD is designed to shift the original pixel grid diagonally by half a pitch length, so a new pixel grid with doubled pixel density is realized, as depicted in Fig. 8(b).

By synchronizing the PBD and computationally generated sub-frames for the original and shifted pixel grids, an image with doubled resolution can be displayed, as shown in Fig. 9. Because of the increased pixel density, the boundaries in the resolution-enhanced image are much smoother than those in the original system. Moreover, the screen-door effect is also minimized since the black matrix between the original pixels is overlapping with the shifted pixels.

##### 2. Foveated Image Shifter

Foveated display is another promising way to deal with limited pixel density utilizing the spatial-varying resolution of the human vision system. Since most of the image receptors

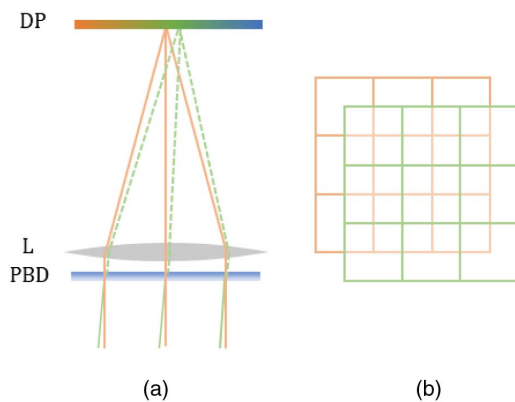


**Fig. 8.** (a) Schematic illustration of the optical system for pixel density enhancement with a PBD. (b) The generation of a half-pitch pixel grid by overlapping the original (orange) and shifted (green) pixel grid. (DP, display panel; L, magnifying lens.)

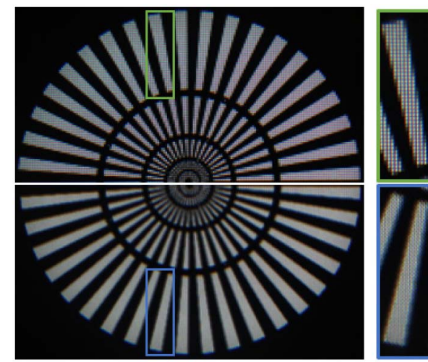


**Fig. 9.** Observed images from the near-eye display system with (lower) and without (upper) pixel density enhancement enabled by a PBD.

(“cone cells”) in the retina are located at a tiny spot called the fovea, human visual acuity is the highest in the center sharp vision zone but drops rapidly when away from the fovea. As a result, the images captured by human eyes are of higher resolution in the fovea region. Regarding immersive display like VR, the information displayed outside the fovea region does not need to keep the same high resolution. This foveated concept has been utilized in some optical designs [75–77] to provide high resolution in a relatively small part but not the full FOV, which could help deal with the pixel density issue and avoid putting a heavy burden on display driving circuits and data transfer rate. Because of the possible shifting of the focused region in the full FOV, an image shifter is usually integrated to

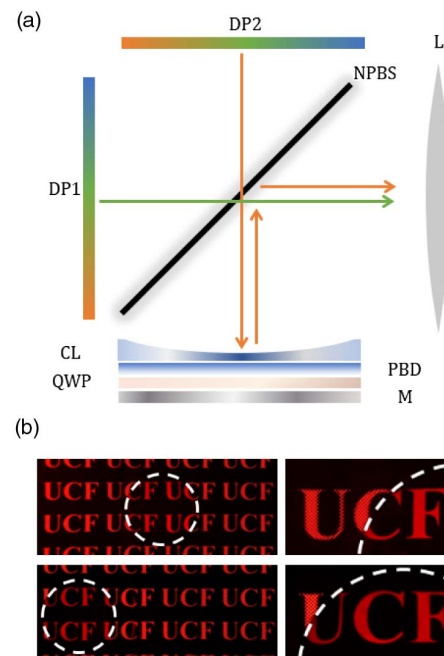


**Fig. 10.** (a) Schematic diagram of a foveated near-eye display system. (DP, display panel; NPBS, non-polarizing beam splitter; CL, concave lens; QWP, quarter-wave plate; M, mirror; L, lens.) (b) Photography of foveated images from the near-eye display system before (upper) and after (lower) image shifting using a PBD.

steer the high-resolution foveated image to the focused area. Figure 10(a) shows a foveated VR display system [78] with a switchable PBD as the image shifter. The image content on display panel 1 (DP1) is directly transmitted to the viewer after passing through the BS and eyepiece (L), while the image displayed on the other panel (DP2) is first condensed by a concave lens (CL) before being reflected to the viewer. With a switchable PBD, the high-resolution foveated image content from DP2 could be shifted, as shown in Fig. 10(b). The fast response (<1 ms) of the PBD could help decrease the latency with eye tracking, and the PBD's high diffraction efficiency (>95%) would also help eliminate ghost images.

**B. PB Lens**

*1. Multiplane Display*

Conventional 3D displays usually provide 3D sensation to viewers by displaying different images to each eye, addressing the vergence cue of the human vision system but ignoring the accommodation cue [79,80]. The mismatch between these two cues can hinder visual performance and cause significant visual fatigue. To minimize the discomfort caused by vergence-accommodation conflict (VAC) [81,82], various types of 3D displays with multiple physical depths have been developed [83–89]. The switchable optical power, intrinsic polarization dependency, compact form factor, and high optical quality of the PBL makes it a suitable adaptive optical element for multiplane displays.

PBLs can be employed in several ways to resolve the VAC [90,91]. By exploiting the fast switchable nature of PBLs, as summarized in Table 1, the displayed image depth could be changed in a time-sequential manner to provide the right accommodation cue dynamically by switching the PBL or the polarization of light. This method could realize a multiplane display using a 2D display panel, but with a considerable burden on the display refresh rate due to time multiplexing.

By making full use of PBLs' polarization dependency, a static method operating in a polarization-multiplexing way [92] is also possible to simultaneously enable two focal depths. Figure 11(a) illustrates a typical optical system for this case. The polarization states of light from each pixel emitted from the display panel (DP) is tuned by the polarization modulation layer (PML) on a pixel-by-pixel level such that the depth information is encoded in the TE to TM ratio for each pixel. After passing through a QWP, the beam's TE to TM ratio is converted to an RCP-to-LCP ratio, as shown in Fig. 11(b). Since the PBL manifests opposite optical power for RCP and LCP, the light from each pixel will be separated into two virtual panels (VPs), depending on its polarization states. Although an additional active-matrix PML is needed, polarization multiplexing could decrease the refresh rate by one-half while displaying the same focal depths, in comparison with time multiplexing. It is noteworthy that both operation methods mentioned above could be easily combined to satisfy different needs in various application scenarios, and the polarization-multiplexing approach could also be employed to drive PBDs for increasing the pixel density.

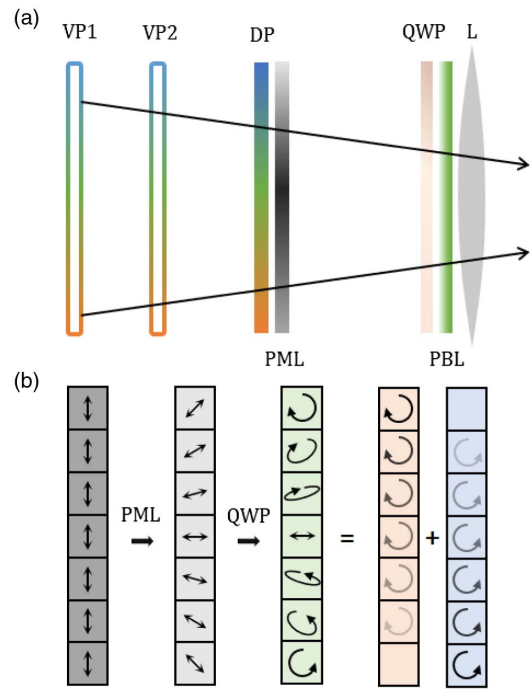


**Fig. 11.** (a) Schematic diagram of a polarization-multiplexed two-plane near-eye display system. (DP, display panel; VP, virtual plane; PML, polarization management layer; QWP, quarter-wave plate; L, lens.) (b) Schematic illustration of polarization change in the polarization multiplexed system.

*2. Reducing Chromatic Aberration*

Conventional refractive lenses using dynamic phase usually have positive (or normal) dispersion, which means the refractive index decreases as the wavelength increases [Fig. 12(a)]. However, since PBLs are essentially diffractive waveplates patterned with parabolic phase variation, they usually manifest negative (or abnormal) dispersion like diffractive optics [Fig. 12(b)]. Thus, PBLs could be integrated into display systems to compensate for the positive dispersion of conventional

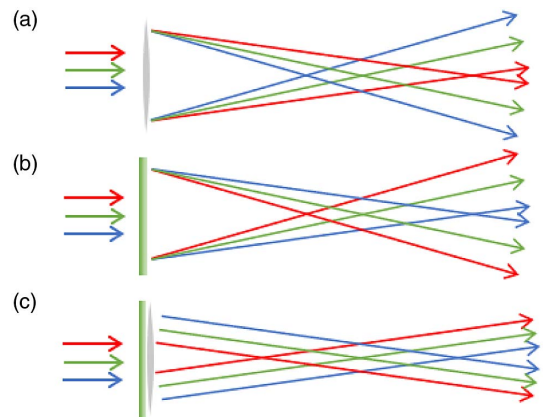


**Fig. 12.** Schematic illustrations of different dispersion scenarios: (a) positive chromatic dispersion in a refractive lens, (b) negative dispersion in a PBL, and (c) zero dispersion in a compensated hybrid optical system.

lenses and thus reduce the chromatic aberration of the whole system [Fig. 12(c)] [38,93,94]. Although achromatic doublet lens sets could also reduce chromatic aberrations, their form factor, weight, and cost may not be acceptable for head-mounted near-eye display systems. The color break-up at the edge of the FOV could be digitally corrected in VR displays, but the extra rendering process may considerably increase computation and power consumption and cause further image latency, particularly for those with large pixel numbers. Integration of a compact and low-cost PBL into head-mounted display systems could be an effective and practical solution for chromatic aberration correction in immersive near-eye displays.

## C. Bragg PBD

### 1. See-Through Optical Combiner

In emerging head-up displays (HUDs) developed for the automobile and aviation industries, high-quality optical combiners are usually employed to redirect the images from the projector to overlap with the see-through FOV. Relatively narrowband combiners that reflect monochromatic light from the light engine are preferred, since in this case the see-through quality may not be significantly altered. Compared to transmissive PBDs, reflective PBDs ( $r$ -PBDs) manifest higher sensitivity in wavelength response. The reflection band of Bragg  $r$ -PBDs could be easily tuned by using LCs with different birefringence, as shown in Fig. 13. Usually, the reflection band is narrower for LCs with smaller birefringence. The diffraction efficiency of  $r$ -PBDs can also be tailored merely by changing the grating layer thickness [14,39] for different application cases. Moreover, it was also shown that PBOEs can be fabricated on non-uniform surfaces or flexible substrates [63]. Thus, it is possible to integrate  $r$ -PBDs to various types of windshields, even with curved surfaces.

### 2. Waveguide Display Couplers

Augmented reality see-through near-eye displays [95,96] and automobile HUDs [97,98] based on waveguide structures have been developed due to their compact form factors. Generally, an input grating coupler is first employed to diffract the display image to a large angle such that the light is constrained in the thin glass plate due to total internal reflection (TIR). An output grating coupler is placed at the see-through end to extract the

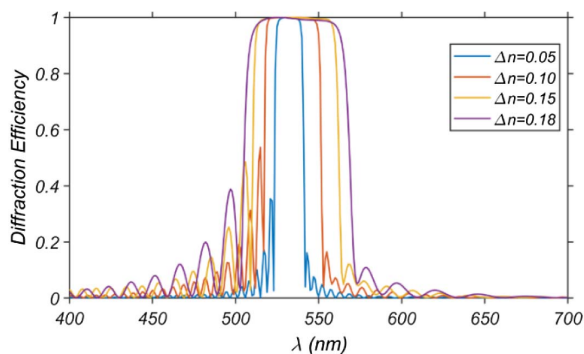


**Fig. 13.** Simulated first-order diffraction efficiency of  $r$ -PBDs ( $\Lambda_x = 678$  nm,  $\Lambda_z = 182$  nm) with different birefringence.

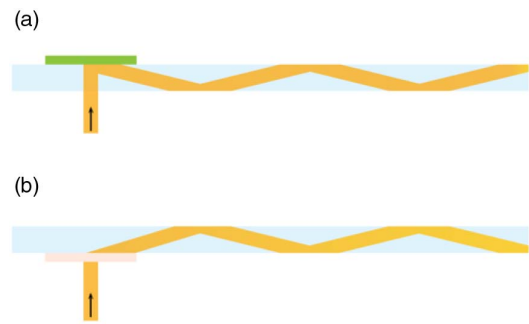


**Fig. 14.** Schematic diagram of the input coupling regime employing (a)  $r$ -PBD and (b) Bragg  $t$ -PBD in see-through display systems based on the waveguide structure.

TIR-guided display light out toward the human eye. As a critical component in waveguide displays, the input grating couplers must have a large diffraction angle with high diffraction efficiency and cover a decent FOV. Also, other diffraction orders should be minimized since they may become unwanted background noise and thus hinder the image quality in the output end. As Bragg gratings, both reflective and transmissive Bragg PBDs ( $r$ - and  $t$ -PBDs) could be employed as the input coupler for waveguide display applications, as shown in Fig. 14. Both types of polarization volume gratings could provide nearly 100% first-order diffraction efficiency with a large deflection angle [14]. Unlike thickness-sensitive Bragg  $t$ -PBDs, the diffraction efficiency of  $r$ -PBDs saturates rapidly to 100% as the grating thickness increases to several micrometers, which is easier for fabrication as input couplers.

In a waveguide-based display system, an eye box with decent size in both lateral and vertical directions is necessary for the eye to capture light from the output coupler. As a result, an exit pupil expander (EPE) [99–101] is commonly deployed in the waveguide display systems. A typical way to expand the exit pupil is to use an output coupler with gradient diffraction efficiency. As the beam is traversing through the waveguide, its intensity drops when it encounters the output coupler. Thus, increasing diffraction efficiency is needed to maintain uniform output intensity, as Fig. 15(a) illustrates. EPEs made of holographic volume gratings or surface relief gratings using

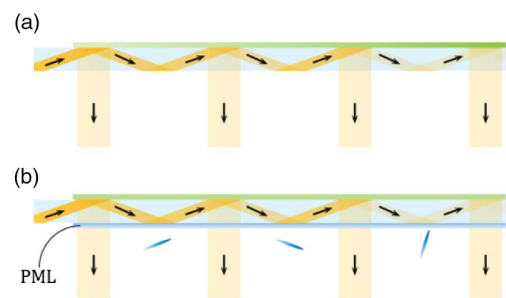


**Fig. 15.** Schematic illustration of exit pupil expansion in the waveguide-based display systems using (a) a gradient-efficiency output grating coupler and (b) a uniform-efficiency output grating coupler with a PML.

this gradient-efficiency approach have been well-developed in commercial products.

Although the gradient-efficiency approach is also applicable for waveguides using *r*-PBD couplers, it is also worth mentioning that since the diffraction efficiency of PBDs is highly sensitive to the input polarization states, another approach based on a PML could also be deployed for exit pupil expansion [91]. The PML is essentially a transparent LC film that has different azimuthal angles at different locations, as shown in Fig. 15(b). Every time the light passes through the PML, its polarization state is tuned such that the desired amount of light will be coupled out at the next contact with the output coupler. By designing the optical axis (azimuthal angle) of LC orientation in the PML and its thickness, the uniformity of output intensity along the whole outcoupling region could be well controlled. Using the polarization-management approach, instead of the gradient-efficiency approach, allows a relatively uniform transmittance of the environmental light, so the EPE region may not manifest gradient transmittance in appearance. Moreover, such a PML is applicable not only for PBD couplers but also for gratings couplers with high polarization sensitivity.

#### 4. PERFORMANCE ENHANCEMENT

##### A. Achromatically High Efficiency

###### 1. LC Birefringence Dispersion

For practical display applications, the diffraction efficiency of PBDs and PBLs in the Raman–Nath region needs to be sufficiently high in the whole visible spectrum or at least for the wavelengths of RGB primary colors, say 630 nm, 532 nm, and 467 nm in the Rec. 2020 system [102]. Otherwise, ghost images caused by zero-order leakage may severely deteriorate the display quality.

In the simplest type of PBOEs, the LC axis orientation has a desired PB pattern in the lateral direction but is homogeneous in the axial direction, where the first-order diffraction efficiency  $\eta$  with circularly polarized input could be theoretically expressed as [103]:

$$\eta = \sin^2\left(\frac{\pi\Delta n d}{\lambda}\right), \quad (3)$$

where  $\Delta n$  is the LC birefringence,  $d$  is the PBOE thickness, and  $\lambda$  is the operating wavelength. In the off-resonance region, the LC birefringence dispersion can be expressed as [104]

$$\Delta n = G \frac{\lambda^2 \lambda^{*2}}{\lambda^2 - \lambda^{*2}}, \quad (4)$$

where  $G$  is the proportionality constant and  $\lambda^*$  is the mean resonance wavelength. Although the LC birefringence decreases as the temperature increases, this effect is not substantial in PBOEs made of LC polymers. In principle, to maintain an achromatically high diffraction efficiency, the  $\Delta n/\lambda$  in Eq. (3) cannot undergo significant variation in the visible spectrum. However, according to Eq. (4), the LC birefringence usually decreases as the wavelength increases in the visible region, which makes the diffraction efficiency even more chromatic. Aimed at enhancing the spectral response of PBOEs, LC materials with shorter  $\lambda^*$  are preferred, so the birefringence dispersion in the visible spectrum can be minimized, as

Fig. 16(a) shows. Another way to enlarge the high-efficiency spectral range is using two kinds of LC materials with different resonance wavelengths. The LC axis orientations in the two layers are orthogonal to each other such that the effective birefringence can be shown as

$$\Delta n_{\text{eff}} = \alpha G_a \frac{\lambda^2 \lambda_a^{*2}}{\lambda^2 - \lambda_a^{*2}} - (1 - \alpha) G_b \frac{\lambda^2 \lambda_b^{*2}}{\lambda^2 - \lambda_b^{*2}}, \quad (5)$$

where  $\alpha$  is the relative thickness of the two LC layers, and  $G_{a,b}$  and  $\lambda_{a,b}^*$  represent the proportionality constant and resonance wavelength of two different LC materials, respectively. In theory, this approach could enable 100% diffraction efficiency at two different wavelengths, and effectively enlarge the high-efficiency spectral range.

Recently, a polymerizable LC mixture with nearly achromatic retardation was reported [105,106] that provides a promising way to fabricate broadband PBOEs with just a single non-twist layer, as shown in Fig. 16(b).

###### 2. Twisted LC Director

In spite of engineering the LC birefringence dispersion, it is also possible to achieve nearly 100% efficiency over a broader spectral range by using a conventional LC material with a twisted

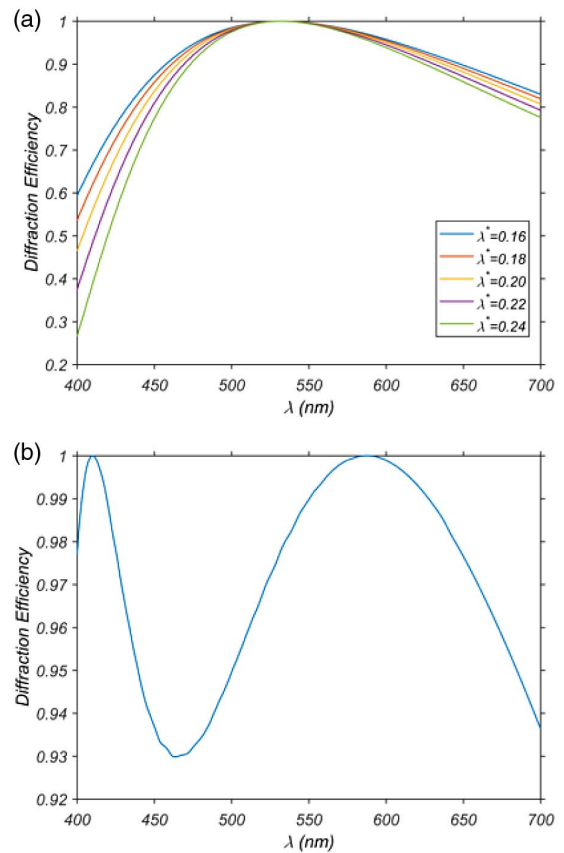


**Fig. 16.** (a) Simulated first-order diffraction efficiency of PBOEs made of LC materials with different resonance wavelengths, where the axial thicknesses are optimized for the half-wave condition at 532 nm. (b) The simulated diffraction efficiency of PBOEs made of negative dispersion LC materials, wherein the birefringence data is from [105].

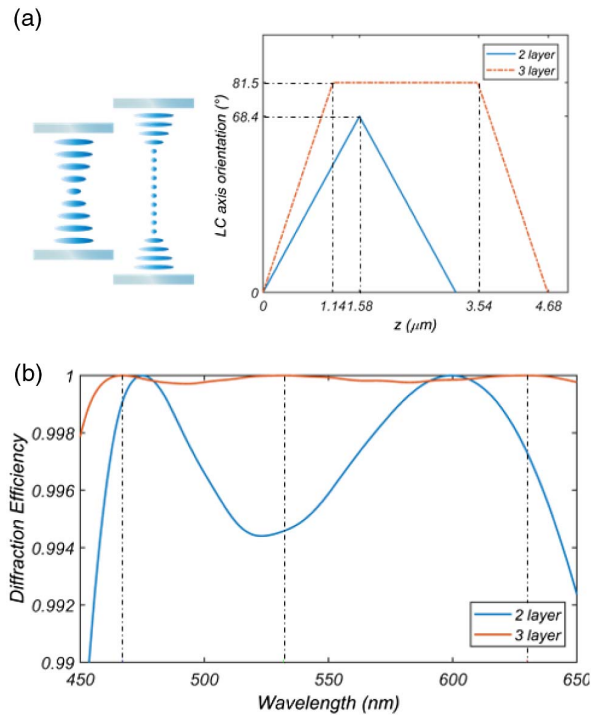


**Fig. 17.** (a) Schematic illustration of the LC orientation in the dual-twist and the sandwich structure. (b) The simulated first-order diffraction efficiency of PBOEs made of two-layer dual-twist and three-layer sandwich structure, optimized for the highest average efficiency at three RGB primary colors (630, 532, and 467 nm) in Rec. 2020.

director orientation in the axial direction. The direction and amplitude (also referred to as helix twisted power) of twisted LC orientation could be well-controlled by adding chiral dopants into LC mixtures. The symmetric dual-twist structure developed by Oh and Escuti [11,107] can effectively enlarge the high-efficiency bandwidth to cover the majority of the visible spectrum. With a three-layer structure, wherein a non-twist layer is sandwiched by two symmetrically twisted layers, PBOEs could be optimized to provide 100% diffraction efficiency in theory at the three RGB primary colors. Figure 17 shows the optimized two-layer and three-layer structures for RGB primary wavelengths and their simulated efficiency over the visible spectrum. The optimization is based on typical birefringence data with  $G = 2.4 \mu\text{m}^{-2}$  and  $\lambda^* = 0.23 \mu\text{m}$  in Eq. (4). Broader bandwidth may be achieved by using more complex twisted multi-layers, principally similar to the design for broadband waveplate retarders [108]. The three-layer sandwiched structure is already more than acceptable for most display applications. The structure parameters in the fabrication process, such as the film thickness and LC twist rate, can be precisely controlled by tuning the spin-coating speed and chiral dopant concentration. Even with a slight deviation from the optimal parameter condition, the diffraction efficiency over the visible spectrum is still tolerable, as shown in Ref. [21].

### B. Wide Field of View

For Bragg PBDs working as waveguide display couplers, high coupling efficiency over a relatively large incident angle is

necessary to provide virtual images with a decent FOV for viewers. However, due to its Bragg nature, the angular bandwidth of a Bragg PBD is usually much more sensitive than that of PBOEs in the Raman–Nath region. To deal with this issue, designs based on twist structures in the axial direction have been developed for both Bragg  $r$ -PBDs and  $t$ -PBDs. Based on the experience on cholesteric LCs [109], a gradient-pitch method was proposed for  $r$ -PBDs in a simulation work [39]. The gradient pitch in the axial direction could effectively enlarge the high-efficiency Bragg condition range of the whole grating, thus resulting in a broader angular and spectral response. More recently, a two-layer twisted Bragg  $t$ -PBD was designed and fabricated [110], in which each layer is a Bragg  $t$ -PBD with the same deflection angle but different slanted angles.

### C. RGB Achromatic Focal Length

Although the chromatic aberration of diffractive PBLs could be compensated by conventional refractive optical elements, PBLs with achromatic focal length for RGB wavelengths are still of great interest for their compact form factor and low cost. Because of the diffractive nature of PBLs, the optical powers of a PBL at the RGB wavelengths are related by

$$\frac{\lambda_r}{K_r} = \frac{\lambda_g}{K_g} = \frac{\lambda_b}{K_b}, \quad (6)$$

where  $K_{r,g,b}$  are the optical powers at the primary RGB colors  $\lambda_{r,g,b}$ . Taking advantage of the polarization-handedness-dependent optical power of PBLs, a method using a stack of PBLs and monochromatic HWPs was demonstrated [111]. For RGB wavelengths, three PBLs and two HWPs are needed, as depicted in Fig. 18. The HWPs here offer retardation only to a single primary color and leave the other two passing unaffected. Based on this configuration, achromatic imaging of RGB wavelengths could be achieved.

Moreover, another method of directly stacking three PBLs with same optical power but at three primary colors was developed [93]. The spectral response of each PBL is tailored to manifest high efficiency at one primary wavelength but low efficiency at the other two, such that each PBL functions for only one primary color.

### D. Fast Response

For an active switchable PBOE, the LC director response time ( $\tau$ ) is determined by the following equations [50,112]:

$$\tau_0 = \frac{\gamma_1 d^2}{K_{11} \pi^2}, \quad (7)$$

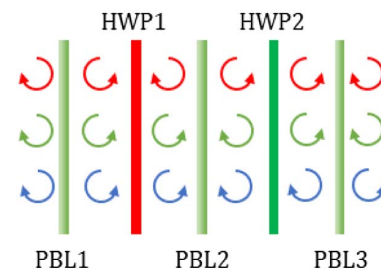


**Fig. 18.** Schematic diagram of the 3-PBL and 2-HWP system with corrected chromatic aberration for the RGB primary colors.

**Table 2. Physical Properties of LCs and Corresponding Response Time of PBD Samples at  $T = 22^\circ\text{C}$  and  $\lambda = 633\text{ nm}$**

LCs	$\Delta n$	$\gamma_1/K_{11}$ ( $\text{ms}/\mu\text{m}^2$ )	$V_{\text{on}}$ ( $V_{\text{rms}}$ )	$\tau_{\text{on}}$ (ms)	$\tau_{\text{off}}$ (ms)
E7	0.21	15.38	7	0.51	3.25
DIC-LC2	0.11	2.54	8	0.39	0.98
HEF951800100 <sup>a</sup>	0.21	N/A	25	0.35	0.55

<sup>a</sup>From Ref. [115],  $\lambda = 671\text{ nm}$ .

$$\tau_{\text{on}} = \frac{\tau_0}{(V/V_{\text{th}})^2 - 1}. \quad (8)$$

In Eqs. (7) and (8),  $\tau_0$  stands for the free relaxation time of LC directors,  $\gamma_1/K_{11}$  is the visco-elastic constant,  $d$  is cell thickness,  $V_{\text{th}}$  is threshold voltage, and  $V$  is the applied voltage. To shorten the response time of PBOEs, a straightforward approach is to decrease the LC layer thickness  $d$ , which requires a higher birefringence ( $\Delta n$ ) LC to satisfy  $d\Delta n = \lambda/2$ . However, a higher  $\Delta n$  LC usually exhibits a stronger wavelength dispersion [113], which in turn leads to a more pronounced efficiency loss in PBOEs. The second approach is to reduce the visco-elastic constant of LC so that the response time can be improved linearly. The third approach is to employ a dual-frequency liquid crystal (DFLC) [114]. Although sub-millisecond response time can be achieved by applying voltage during both turn-on and turn-off processes, the problems are the increased driving voltage and dielectric heating effect of the LC.

To measure the response time of a PBOE (e.g., PBD), we positioned a linear polarizer after a laser source (e.g., He-Ne laser,  $\lambda = 633\text{ nm}$ ) and sent the beam to the PBD samples at normal incidence. An iris was placed 0.5 m away from the PBD with a photodetector following. For a nematic LC-based PBD, in the voltage-off state, the LC directors followed the surface alignment, and the light was deflected and received by the photodetector. When a longitudinal electric field was turned on, the LC directors were reoriented to be vertical to the substrate. As a result, the incident light experienced no phase change, and the light was not deflected so that it was blocked by the iris. For a DFCLC-based PBD, voltages were always applied on the device, and the turn-on/turn-off processes were achieved by changing the driving frequency. The response time was calculated between the recorded 10% and 90% transmittance change. Table 2 lists the measured turn-on ( $\tau_{\text{on}}$ ) and turn-off time ( $\tau_{\text{off}}$ ) of three PBD samples based on two nematic LCs (E7 and DIC-LC2 [116]) and one DFCLC (HEF951800100 [115]). As discussed above, the low  $\gamma_1/K_{11}$  of DIC-LC2 ( $\sim 2.54$ ) helps to achieve faster response time than that of E7 at a relatively low driving voltage, while for HEF951800100, although it exhibits submillisecond response time, its required voltage is higher.

## 5. SIMULATION METHODS

### A. Matrix Solvers

The well-known 2-by-2 Jones matrix method, also referred to as the Jones calculus, is a simple and effective analysis tool for

PBOEs in the Raman–Nath region. The Jones matrix method, which characterizes the polarizing effect of the optical element by a 2-by-2 matrix, has been extensively used to investigate the spectral response of PBOEs due to its simplicity [107]. Similarly, the Muller calculus, a generalization of the Jones calculus that uses a 4-by-4 matrix to transfer the Stokes vector of input light to the output side, could also be employed to analyze PBOEs [108] with a partially polarized input. Although the Jones and Muller matrix methods can handle the optical response of PBOEs only at normal incidence, their concise formulation and fast calculation speed may help give some useful insights for the spectral response of PBOEs. For oblique incidence, an extended 2-by-2 matrix method [117] and a Berreman 4-by-4 matrix method [118] could be used to model PBOEs. However, their application scope should be cautiously limited to the Raman–Nath region, where the in-plane wave interaction should be negligible.

### B. Finite-Difference Time-Domain

For the investigation of spectral and angular responses of PBOEs with a large deflection angle, the finite-difference time-domain method (FDTD) can be exploited. FDTD, or Yee's method [119], is one of the most robust and accessible methods to numerically calculate electromagnetic wave propagation in numerous photonic devices, including both periodic and non-periodic structures. Even though FDTD, as a grid-based finite difference analysis method, is considerably more time- and memory- consuming than matrix solvers, it can handle oblique incidence and conveniently produce the spectral response of complex structures. Theoretically, FDTD could analyze arbitrary LC-based PBOEs, including but not limited to PBDs and PBLs, with normal or oblique incidence. With the rapid development of optics and photonics, FDTD has been extensively improved by motivated scientists and engineers for broader implementation scope [120,121] with faster and more accurate computation [122,123].

Although many commercial 2D/3D Maxwell's solvers, such as Lumerical FDTD solutions, are now available with graphic user interface, the FDTD analysis of PBDs was first developed by Oh and Escuti [124] and then generalized to 3D conical incidence by Miskiewicz *et al.* [125], whose source codes in standard C/C++ format are generously shared online with the name “WOLFSIM (Wideband Optical FDTD Simulator).”

### C. Finite-Difference Frequency-Domain

Finite-difference frequency-domain (FDFD) [126–128] is another popular numerical analysis method in photonics, which can produce very accurate electromagnetic field distributions for a single time harmonic. FDFD exhibits several advantages over FDTD for the analysis of PBOEs if the transient state of the electromagnetic wave propagation is not required. First, FDFD usually takes a relatively long time to achieve a steady state, which can be done immediately by FDFD. Second, since the Courant–Friedrichs–Lewy condition is necessary for accurate results in FDTD, the constant time-step is troublesome where small length interval is required. Also, FDTD usually uses fitted material dispersion after Fourier transform, but FDFD directly employs the measured material dispersion,

which is more convenient and accurate for field applications. Commonly, FDTD is more opportune to find the approximate resonance locations in the spectrum due to its time-domain nature, while the single-frequency analysis of the results from FDFD can help to visualize the distinct field distributions at resonance wavelengths inside or close to the structures. The finite element method (FEM) [129], another more complicated frequency-domain Maxwell's solver, can model curved objects better than FDFD, but it is not necessary for the analysis of PBOEs considering their flat geometries. Also, the FDFD is significantly more straightforward to implement and modify than FEM. Interested users may easily develop an FDFD tool for the analysis of PBOEs based on the well-known formulations or just by adding an anisotropy feature to existing ones.

#### D. Rigorous Coupled Wave Analysis

For periodic structures, the rigorous coupled wave analysis (RCWA) developed by Moharam and Gaylord [130] is one of the most powerful and popular simulation tools that can be applied to solve scattering behaviors. RCWA was first developed to study holographic gratings and then successfully extended to surface-relief gratings and complex multilayer grating structures. In the past decades, extensive work has been done to improve the stability and convergence of RCWA [131–133] and extend it to much broader applications [134–140]. RCWA represents both materials and fields as spatial harmonics, so it is extraordinarily fast and accurate for devices with low to moderate permittivity variations.

The detailed 3D vectorial RCWA formulation of anisotropic gratings with arbitrary permittivity matrix was already developed in the last century [137]. Because of the simplicity of linearly periodic PBOEs with a constant amplitude of birefringence, the permittivity matrix can be flawlessly described by three spatial harmonics. With increasing attention of PBOEs in recent years, the analysis of periodic PBDs based on RCWA was conducted and compared with FDTD [141–143]. As a semi-analytical numerical method, RCWA can simulate the diffraction efficiency of periodic PBOEs at both normal and oblique incidence with the same accuracy but much faster speed, making it more convenient to optimize for desired performance.

## 6. SUMMARY

Recent advances in the fabrication and simulation of liquid-crystal-based Pancharatnam–Berry phase optical elements and their applications for emerging display systems are briefly reviewed. With the development of advanced liquid crystal materials and polarization holography methods, various kinds of PBOEs with high-grade quality have been demonstrated. Because of the characteristic polarization dependency and high diffraction efficiency of PBOEs, they have been successfully integrated into optical systems to satisfy the increasing needs from next-generation display systems, such as near-eye displays for augmented/virtual/mixed reality and head-up displays for automobile and aviation. Continuing and substantial progress in this field with novel material and structure designs should be expected, which would hopefully motivate faster evolving of next-generation display systems from scientific research, military defense, and industry production to our daily life.

**Funding.** Intel Corporation; GoerTek Electronics.

**Acknowledgment.** The authors would like to thank Dr. Ronald Azuma (Intel Labs), Prof. M. G. Moharam (CREOL), and Prof. Yan Li (Shanghai Jiao Tong University) for useful discussion.

## REFERENCES

1. B. E. Saleh and M. C. Teich, *Fundamentals of Photonics* (Wiley, 2007).
2. M. Born and E. Wolf, *Principles of Optics: Electromagnetic Theory of Propagation, Interference and Diffraction of Light* (Elsevier, 2013).
3. S. D. Kakichashvili, "Hologram polarization recording (holographic image polarization recording and sum wave simulation on photoanisotropic materials, using Weigert effect)," *Opt. Spektrosk.* **33**, 324–327 (1972).
4. M. Attia and J. M. Jonathan, "Anisotropic gratings recorded from two circularly polarized coherent waves," *Opt. Commun.* **47**, 85–90 (1983).
5. T. Todorov, L. Nikolova, and N. Tomova, "Polarization holography. 1: A new high-efficiency organic material with reversible photoinduced birefringence," *Appl. Opt.* **23**, 4309–4312 (1984).
6. T. Todorov, L. Nikolova, and N. Tomova, "Polarization holography. 2: Polarization holographic gratings in photoanisotropic materials with and without intrinsic birefringence," *Appl. Opt.* **23**, 4588–4591 (1984).
7. I. D. Shatalin, S. D. Kakichashvili, and V. I. Kakichashvili, "A polarization hologram with a 100-percent diffraction efficiency (a polarization cineform)," *Pisma v Zh. Tekhnicheskoi Fiz.* **13**, 1051–1055 (1987).
8. L. Marrucci, C. Manzo, and D. Paparo, "Pancharatnam-Berry phase optical elements for wave front shaping in the visible domain: switchable helical mode generation," *Appl. Phys. Lett.* **88**, 221102 (2006).
9. L. Nikolova and P. S. Ramanujam, *Polarization Holography* (Cambridge Univ. Press, 2009).
10. M. G. Moharam and L. Young, "Criterion for Bragg and Raman-Nath diffraction regimes," *Appl. Opt.* **17**, 1757–1759 (1978).
11. C. Oh and M. J. Escuti, "Achromatic diffraction from polarization gratings with high efficiency," *Opt. Lett.* **33**, 2287–2289 (2008).
12. J. Kobashi, H. Yoshida, and M. Ozaki, "Planar optics with patterned chiral liquid crystals," *Nat. Photonics* **10**, 389–392 (2016).
13. K. Gao, C. McGinty, H. Payson, S. Berry, J. Vornehm, V. Finnemeyer, B. Roberts, and P. Bos, "High-efficiency large-angle Pancharatnam phase deflector based on dual-twist design," *Opt. Express* **25**, 6283–6293 (2017).
14. Y.-H. Lee, K. Yin, and S.-T. Wu, "Reflective polarization volume gratings for high efficiency waveguide-coupling augmented reality displays," *Opt. Express* **25**, 27008–27014 (2017).
15. X. Xiang, J. Kim, R. Komanduri, and M. J. Escuti, "Nanoscale liquid crystal polymer Bragg polarization gratings," *Opt. Express* **25**, 19298–19308 (2017).
16. J. Kim, Y. Li, M. N. Miskiewicz, C. Oh, M. W. Kudenov, and M. J. Escuti, "Fabrication of ideal geometric-phase holograms with arbitrary wavefronts," *Optica* **2**, 958–964 (2015).
17. O. Sakhno, Y. Gritsai, H. Sahn, and J. Stumpe, "Fabrication and performance of efficient thin circular polarization gratings with Bragg properties using bulk photo-alignment of a liquid crystalline polymer," *Appl. Phys. B* **124**, 52 (2018).
18. F. Gou, F. Peng, Q. Ru, Y.-H. Lee, H. Chen, Z. He, T. Zhan, K. L. Vodopyanov, and S.-T. Wu, "Mid-wave infrared beam steering based on high-efficiency liquid crystal diffractive waveplates," *Opt. Express* **25**, 22404–22410 (2017).
19. E. Hasman, V. Kleiner, G. Biener, and A. Niv, "Polarization dependent focusing lens by use of quantized Pancharatnam-Berry phase diffractive optics," *Appl. Phys. Lett.* **82**, 328–330 (2003).
20. K. Gao, H.-H. Cheng, A. K. Bhowmik, and P. J. Bos, "Thin-film Pancharatnam lens with low f-number and high quality," *Opt. Express* **23**, 26086–26094 (2015).
21. N. V. Tabiryan, S. V. Serak, S. R. Nersisyan, D. E. Roberts, B. Y. Zeldovich, D. M. Steeves, and B. R. Kimball, "Broadband waveplate lenses," *Opt. Express* **24**, 7091–7102 (2016).

22. K. Gao, H.-H. Cheng, A. Bhowmik, C. McGinty, and P. Bos, "Nonmechanical zoom lens based on the Pancharatnam phase effect," *Appl. Opt.* **55**, 1145–1150 (2016).
23. K. J. Hornburg, X. Xiang, J. Kim, M. Kudenov, and M. Escuti, "Design and fabrication of an aspheric geometric-phase lens doublet," *Proc. SPIE* **10735**, 1073513 (2018).
24. X. Xiang, M. Kudenov, M. Escuti, and K. J. Hornburg, "Optimization of aspheric geometric-phase lenses for improved field-of-view," *Proc. SPIE* **10743**, 1074305 (2018).
25. N. V. Tabiryán, S. V. Serak, D. E. Roberts, D. M. Steeves, and B. R. Kimball, "Thin waveplate lenses of switchable focal length—new generation in optics," *Opt. Express* **23**, 25783–25794 (2015).
26. T. Zhan, J. Xiong, Y.-H. Lee, and S.-T. Wu, "Polarization-independent Pancharatnam-Berry phase lens system," *Opt. Express* **26**, 35026–35033 (2018).
27. M. Fratz, S. Sinzinger, and D. Giel, "Design and fabrication of polarization-holographic elements for laser beam shaping," *Appl. Opt.* **48**, 2669–2677 (2009).
28. S. C. McEldowney, D. M. Shemo, R. A. Chipman, and P. K. Smith, "Creating vortex retarders using photoaligned liquid crystal polymers," *Opt. Lett.* **33**, 134–136 (2008).
29. D. Mawet, E. Serabyn, K. Liewer, C. Hanot, S. McEldowney, D. Shemo, and N. O'Brien, "Optical vectorial vortex coronagraphs using liquid crystal polymers: theory, manufacturing and laboratory demonstration," *Opt. Express* **17**, 1902–1918 (2009).
30. S. R. Nersisyan, N. V. Tabiryán, D. Mawet, and E. Serabyn, "Improving vector vortex waveplates for high-contrast coronagraphy," *Opt. Express* **21**, 8205–8213 (2013).
31. S. Slussarenko, S. Murauski, T. Du, V. Chigrinov, L. Marrucci, and E. Santamato, "Tunable liquid crystal q-plates with arbitrary topological charge," *Opt. Express* **19**, 4085–4090 (2011).
32. W. Ji, C. H. Lee, P. Chen, W. Hu, Y. Ming, L. Zhang, T. H. Lin, V. Chigrinov, and Y. Q. Lu, "Meta-q-plate for complex beam shaping," *Sci. Rep.* **6**, 25528 (2016).
33. P. Chen, Y. Q. Lu, and W. Hu, "Beam shaping via photopatterned liquid crystals," *Liq. Cryst.* **43**, 2051–2061 (2016).
34. M. Jiang, H. Yu, X. Feng, Y. Guo, I. Chaganava, T. Turiv, O. D. Lavrentovich, and Q. Wei, "Liquid crystal Pancharatnam-Berry micro-optical elements for laser beam shaping," *Adv. Opt. Mater.* **6**, 1800961 (2018).
35. W. Hu, P. Chen, and Y.-Q. Lu, "Photoinduced liquid crystal domain engineering for optical field control," in *Photoactive Functional Soft Materials: Preparation, Properties, and Applications* (Wiley-VCH Verlag, 2018), pp. 361–387.
36. L. De Sio, D. E. Roberts, Z. Liao, J. Hwang, N. Tabiryán, D. M. Steeves, and B. R. Kimball, "Beam shaping diffractive wave plates," *Appl. Opt.* **57**, A118–A121 (2018).
37. S. V. Serak, D. E. Roberts, J. Y. Hwang, S. R. Nersisyan, N. V. Tabiryán, T. J. Bunning, D. M. Steeves, and B. R. Kimball, "Diffractive waveplate arrays," *J. Opt. Soc. Am.* **34**, B56–B63 (2017).
38. Y.-H. Lee, G. Tan, T. Zhan, Y. Weng, G. Liu, F. Gou, F. Peng, N. V. Tabiryán, S. Gauza, and S.-T. Wu, "Recent progress in Pancharatnam-Berry phase optical elements and the applications for virtual/augmented realities," *Opt. Data Process. Storage* **3**, 79–88 (2017).
39. Y. Weng, D. Xu, Y. Zhang, X. Li, and S.-T. Wu, "Polarization volume grating with high efficiency and large diffraction angle," *Opt. Express* **24**, 17746–17759 (2016).
40. W. M. Gibbons, P. J. Shannon, S. T. Sun, and B. J. Swetlin, "Surface-mediated alignment of nematic liquid crystals with polarized laser light," *Nature* **351**, 49–50 (1991).
41. K. Ichimura, "Photoalignment of liquid-crystal systems," *Chem. Rev.* **100**, 1847–1874 (2000).
42. D. W. Berreman, "Solid surface shape and the alignment of an adjacent nematic liquid crystal," *Phys. Rev. Lett.* **28**, 1683–1686 (1972).
43. V. G. Chigrinov, V. M. Kozenkov, and H. S. Kwok, *Photoalignment of Liquid Crystalline Materials: Physics and Applications*, Vol. 17 of SID Series on Display Technology (Wiley, 2008).
44. T. Seki, S. Nagano, and M. Hara, "Versatility of photoalignment techniques: from nematics to a wide range of functional materials," *Polymer* **54**, 6053–6072 (2013).
45. V. Chigrinov, A. Muravski, H. S. Kwok, H. Takada, H. Akiyama, and H. Takatsu, "Anchoring properties of photoaligned azo-dye materials," *Phys. Rev. E* **68**, 061702 (2003).
46. M. C. Tseng, O. Yaroshchuk, T. Bidna, A. K. Srivastava, V. Chigrinov, and H. S. Kwok, "Strengthening of liquid crystal photoalignment on azo dye films: passivation by reactive mesogens," *RSC Adv.* **6**, 48181–48188 (2016).
47. J. Wang, C. McGinty, R. Reich, V. Finnemeyer, H. Clark, S. Berry, and P. Bos, "Process for a reactive monomer alignment layer for liquid crystals formed on an azodye sublayer," *Materials* **11**, 1195 (2018).
48. J. Wang, C. McGinty, J. West, D. Bryant, V. Finnemeyer, R. Reich, S. Berry, H. Clark, O. Yaroshchuk, and P. Bos, "Effects of humidity and surface on photoalignment of brilliant yellow," *Liq. Cryst.* **44**, 863–872 (2017).
49. E. Ouskova, R. Vergara, J. Hwang, D. Roberts, D. M. Steeves, B. R. Kimball, and N. Tabiryán, "Dual-function reversible/irreversible photoalignment material," *J. Mol. Liq.* **267**, 205–211 (2018).
50. D. K. Yang and S.-T. Wu, *Fundamentals of Liquid Crystal Devices* (Wiley, 2014).
51. R. K. Komanduri, C. Oh, M. J. Escuti, and D. J. Kekas, "18:3: Late-News Paper: Polarization independent liquid crystal microdisplays," *SID Symp. Dig. Tech. Pap.* **39**, 236–239 (2008).
52. C. Decker and K. Moussa, "Real-time kinetic study of laser-induced polymerization," *Macromolecules* **22**, 4455–4462 (1989).
53. S. J. Bryant, C. R. Nuttelman, and K. S. Anseth, "Cytocompatibility of UV and visible light photoinitiating systems on cultured NIH/3T3 fibroblasts in vitro," *J. Biomater. Sci. Polym. Ed.* **11**, 439–457 (2000).
54. D. Kou, G. Manius, H. Tian, and H. P. Chokshi, "Polymers and surfactants," in *Charged Aerosol Detection for Liquid Chromatography and Related Separation Techniques* (Wiley, 2017), pp. 327–339.
55. L. De Sio, D. E. Roberts, Z. Liao, S. Nersisyan, O. Uskova, L. Wickboldt, N. Tabiryán, D. M. Steeves, and B. R. Kimball, "Digital polarization holography advancing geometrical phase optics," *Opt. Express* **24**, 18297–18306 (2016).
56. A. Emoto, T. Matsumoto, A. Yamashita, T. Shioda, H. Ono, and N. Kawatsuki, "Large birefringence and polarization holographic gratings formed in photocross-linkable polymer liquid crystals comprising bistolane mesogenic side groups," *J. Appl. Phys.* **106**, 073505 (2009).
57. H. Ono, A. Emoto, F. Takahashi, N. Kawatsuki, and T. Hasegawa, "Highly stable polarization gratings in photocrosslinkable polymer liquid crystals," *J. Appl. Phys.* **94**, 1298–1303 (2003).
58. R. Rosenhauer, T. Fischer, S. Czaplá, J. Stumpe, A. Viñuales, M. Pinol, and J. L. Serrano, "Photo-induced alignment of LC polymers by photoorientation and thermotropic self-organization," *Mol. Cryst. Liq. Cryst. Sci. Technol. Sect. A* **364**, 295–304 (2001).
59. S. D. Kakichashvili, "Method for phase polarization recording of holograms," *Sov. J. Quantum Electron.* **4**, 795–798 (1974).
60. G. P. Crawford, J. N. Eakin, M. D. Radcliffe, A. Callan-Jones, and R. A. Pelcovits, "Liquid-crystal diffraction gratings using polarization holography alignment techniques," *J. Appl. Phys.* **98**, 123102 (2005).
61. J. Kim, R. K. Komanduri, and M. J. Escuti, "A compact holographic recording setup for tuning pitch using polarizing prisms," *Proc. SPIE* **8281**, 82810R (2012).
62. M. N. Miskiewicz, J. Kim, Y. Li, R. K. Komanduri, and M. J. Escuti, "Progress on large-area polarization grating fabrication," *Proc. SPIE* **8395**, 83950G (2012).
63. C. Oh, "Broadband polarization gratings for efficient liquid crystal display, beam steering, spectropolarimetry, and Fresnel zone plate," Ph.D. dissertation (North Carolina State University, 2009).
64. J. Kim, "Liquid crystal geometric phase holograms for efficient beam steering and imaging spectropolarimetry," Ph.D. dissertation (North Carolina State University, 2011).
65. H. Wu, W. Hu, H. Hu, X. Lin, G. Zhu, J.-W. Choi, V. Chigrinov, and Y. Lu, "Arbitrary photo-patterning in liquid crystal alignments using DMD based lithography system," *Opt. Express* **20**, 16684–16689 (2012).
66. P. Chen, B. Wei, W. Ji, S. Ge, W. Hu, F. Xu, V. Chigrinov, and Y. Lu, "Arbitrary and reconfigurable optical vortex generation: a high-efficiency technique using director-varying liquid crystal fork gratings," *Photon. Res.* **3**, 133–139 (2015).

67. P. Chen, S. J. Ge, W. Duan, B. Y. Wei, G. X. Cui, W. Hu, and Y. Q. Lu, "Digitalized geometric phases for parallel optical spin and orbital angular momentum encoding," *ACS Photon.* **4**, 1333–1338 (2017).
68. M. N. Miskiewicz and M. J. Escuti, "Direct-writing of complex liquid crystal patterns," *Opt. Express* **22**, 12691–12706 (2014).
69. H. Ono, T. Wada, and N. Kawatsuki, "Polarization imaging screen using vector gratings fabricated by photocrosslinkable polymer liquid crystals," *Jpn. J. Appl. Phys.* **51**, 082501 (2012).
70. S. Nersisyan, N. Tabirian, D. M. Steeves, and B. R. Kimball, "Fabrication of liquid crystal polymer axial waveplates for UV-IR wavelengths," *Opt. Express* **17**, 11926–11934 (2009).
71. C. Vieri, G. Lee, N. Balram, S. H. Jung, J. Y. Yang, S. Y. Yoon, and I. B. Kang, "An 18 megapixel 4.3" 1443 ppi 120 Hz OLED display for wide field of view high acuity head mounted displays," *J. Soc. Inf. Disp.* **26**, 314–324 (2018).
72. Y. Iwase, A. Tagawa, Y. Takeuchi, T. Watanabe, S. Horiuchi, Y. Asai, K. Yamamoto, T. Daitoh, and T. Matsuo, "A novel low-power gate driver architecture for large 8 K 120 Hz liquid crystal display employing IGZO technology," *J. Soc. Inf. Disp.* **26**, 304–313 (2018).
73. Y.-H. Lee, T. Zhan, and S.-T. Wu, "Enhancing the resolution of a near-eye display with a Pancharatnam-Berry phase deflector," *Opt. Lett.* **42**, 4732–4735 (2017).
74. Y.-H. Lee, T. Zhan, G. Tan, F. Gou, F. Peng, and S.-T. Wu, "Optical display system with enhanced resolution, methods, and applications," U.S. patent 10115327B1 (October 30, 2018).
75. H. Hua and S. Liu, "Dual-sensor foveated imaging system," *Appl. Opt.* **47**, 317–327 (2008).
76. Y. Qin and H. Hua, "Continuously zoom imaging probe for the multi-resolution foveated laparoscope," *Biomed. Opt. Express* **7**, 1175–1182 (2016).
77. J. P. Rolland, A. Yoshida, L. D. Davis, and J. H. Reif, "High-resolution inset head-mounted display," *Appl. Opt.* **37**, 4183–4193 (1998).
78. G. Tan, Y.-H. Lee, T. Zhan, J. Yang, S. Liu, D. Zhao, and S.-T. Wu, "Foveated imaging for near-eye displays," *Opt. Express* **26**, 25076–25085 (2018).
79. J. Geng, "Three-dimensional display technologies," *Adv. Opt. Photonics* **5**, 456–535 (2013).
80. B. Lee, "Three-dimensional displays, past and present," *Phys. Today* **66**(4), 36–41 (2013).
81. D. M. Hoffman, A. R. Girshick, and M. S. Banks, "Vergence–accommodation conflicts hinder visual performance and cause visual fatigue," *J. Vis.* **8**(3):33 (2008).
82. S. J. Watt, K. Akeley, M. O. Ernst, and M. S. Banks, "Focus cues affect perceived depth," *J. Vis.* **5**(10): 7 (2005).
83. D. Lanman and D. Luebke, "Near-eye light field displays," *ACM Trans. Graph.* **32**, 1–10 (2013).
84. H. S. Park, R. Hoskinson, H. Abdollahi, and B. Stoeber, "Compact near-eye display system using a superlens-based microlens array magnifier," *Opt. Express* **23**, 30618–30632 (2015).
85. C.-K. Lee, S. Moon, S. Lee, D. Yoo, J.-Y. Hong, and B. Lee, "Compact three-dimensional head-mounted display system with Savart plate," *Opt. Express* **24**, 19531–19544 (2016).
86. F.-C. Huang, D. Luebke, and G. Wetzstein, "The light field stereoscope," *ACM Trans. Graph.* **34**, 60 (2015).
87. S. Lee, C. Jang, S. Moon, J. Cho, and B. Lee, "Additive light field displays: realization of augmented reality with holographic optical elements," *ACM Trans. Graph.* **35**, 60 (2016).
88. S. Liu and H. Hua, "A systematic method for designing depth-fused multi-focal plane three-dimensional displays," *Opt. Express* **18**, 11562–11573 (2010).
89. S. Ravikumar, K. Akeley, and M. S. Banks, "Creating effective focus cues in multi-plane 3D displays," *Opt. Express* **19**, 20940–20952 (2011).
90. T. Zhan, Y.-H. Lee, and S.-T. Wu, "High-resolution additive light field near-eye display by switchable Pancharatnam-Berry phase lenses," *Opt. Express* **26**, 4863–4872 (2018).
91. Y. H. Lee, G. Tan, K. Yin, T. Zhan, and S. T. Wu, "Compact see-through near-eye display with depth adaption," *J. Soc. Inf. Disp.* **26**, 64–70 (2018).
92. G. Tan, T. Zhan, Y.-H. Lee, J. Xiong, and S.-T. Wu, "Polarization-multiplexed multiplane display," *Opt. Lett.* **43**, 5651–5654 (2018).
93. D. Roberts, Z. Liao, J. Y. Hwang, S. R. Nersisyan, and N. Tabirian, "Chromatic aberration corrected switchable optical systems," *Proc. SPIE* **10735**, 107350Q (2018).
94. A. Jamali and P. Bos, "A thin film liquid crystal based compensator for the chromatic aberration of optical lenses," *Mol. Cryst. Liq. Cryst.* **657**, 46–50 (2017).
95. Z. Liu, Y. Pang, C. Pan, and Z. Huang, "Design of a uniform-illumination binocular waveguide display with diffraction gratings and freeform optics," *Opt. Express* **25**, 30720–30731 (2017).
96. Y. Weng, Y. Zhang, J. Cui, A. Liu, Z. Shen, X. Li, and B. Wang, "Liquid-crystal-based polarization volume grating applied for full-color waveguide displays," *Opt. Lett.* **43**, 5773–5776 (2018).
97. C. M. Bigler, P.-A. Blanche, and K. Sarma, "Holographic waveguide heads-up display for longitudinal image magnification and pupil expansion," *Appl. Opt.* **57**, 2007–2013 (2018).
98. M. Homan, "The use of optical waveguides in head up display (HUD) applications," *Proc. SPIE* **8736**, 87360E (2013).
99. P. Saarikko, "Diffractive exit-pupil expander with a large field of view," *Proc. SPIE* **7001**, 700105 (2008).
100. P. Äyräs, P. Saarikko, and T. Levola, "Exit pupil expander with a large field of view based on diffractive optics," *J. Soc. Inf. Disp.* **17**, 659–664 (2009).
101. R. Shechter, Y. Amitai, and A. A. Friesem, "Compact beam expander with linear gratings," *Appl. Opt.* **41**, 1236–1240 (2002).
102. R. Zhu, Z. Luo, H. Chen, Y. Dong, and S.-T. Wu, "Realizing Rec 2020 color gamut with quantum dot displays," *Opt. Express* **23**, 23680–23693 (2015).
103. J. Tervo and J. Turunen, "Paraxial-domain diffractive elements with 100% efficiency based on polarization gratings," *Opt. Lett.* **25**, 785–786 (2000).
104. S.-T. Wu, "Birefringence dispersions of liquid crystals," *Phys. Rev. A* **33**, 1270–1274 (1986).
105. E. Beltran, I. Gardiner, and M. Goebel, "Coatable optical films for advanced displays," *SID Symp. Dig.* **48**, 790–792 (2017).
106. S. Yang, H. Lee, and J.-H. Lee, "Negative dispersion retarder with a wide viewing angle made by stacking reactive mesogen on a poly-methylmethacrylate film," *Opt. Eng.* **55**, 027106 (2016).
107. C. Oh and M. J. Escuti, "Achromatic polarization gratings as highly efficient thin-film polarizing beamsplitters for broadband light," *Proc. SPIE* **6682**, 668211 (2007).
108. R. K. Komanduri, K. F. Lawler, and M. J. Escuti, "Multi-twist retarders: broadband retardation control using self-aligning reactive liquid crystal layers," *Opt. Express* **21**, 404–420 (2013).
109. Q. Hong, T. X. Wu, and S. T. Wu, "Optical wave propagation in a cholesteric liquid crystal using the finite element method," *Liq. Cryst.* **30**, 367–375 (2003).
110. X. Xiang, J. Kim, and M. J. Escuti, "Bragg polarization gratings for wide angular bandwidth and high efficiency at steep deflection angles," *Sci. Rep.* **8**, 10–15 (2018).
111. J. Kim, K. J. Hornburg, M. J. Escuti, and N. Z. Warriner, "Chromatic-aberration correction in geometric-phase lenses, for red, green, and blue operation," *Proc. SPIE* **10361**, 1036113 (2017).
112. S.-T. Wu, "Design of a liquid crystal based tunable electrooptic filter," *Appl. Opt.* **28**, 48–52 (1989).
113. J. Li, C.-H. Wen, S. Gauza, R. Lu, and S.-T. Wu, "Refractive indices of liquid crystals for display applications," *J. Disp. Technol.* **1**, 51–61 (2005).
114. H. Xianyu, S. T. Wu, and C. L. Lin, "Dual frequency liquid crystals: a review," *Liq. Cryst.* **36**, 717–726 (2009).
115. W. Duan, P. Chen, B.-Y. Wei, S.-J. Ge, X. Liang, W. Hu, and Y.-Q. Lu, "Fast-response and high-efficiency optical switch based on dual-frequency liquid crystal polarization grating," *Opt. Mater. Express* **6**, 597–602 (2016).
116. Z. Luo, F. Peng, H. Chen, M. Hu, J. Li, Z. An, and S.-T. Wu, "Fast-response liquid crystals for high image quality wearable displays," *Opt. Mater. Express* **5**, 603–610 (2015).
117. C. Gu and P. Yeh, "Extended Jones matrix method. II," *J. Opt. Soc. Am. A* **10**, 966–973 (1982).
118. D. W. Berreman, "Optics in stratified and anisotropic media: 4x4-matrix formulation," *J. Opt. Soc. Am.* **62**, 502–510 (1972).

119. K. S. Yee, "Numerical solution of initial boundary value problems involving Maxwell's equations in isotropic media," *IEEE Trans. Antennas Propag.* **14**, 302–307 (1966).
120. J. Schneider and S. Hudson, "The finite-difference time-domain method applied to anisotropic material," *IEEE Trans. Antennas Propag.* **41**, 994–999 (1993).
121. J. L. Young and R. O. Nelson, "A summary and systematic analysis of FDTD algorithms for linearly dispersive media," *IEEE Antennas Propag. Mag.* **43**(1), 61–126 (2001).
122. R. Holland, "Finite-difference solution of Maxwell's equations in generalized nonorthogonal coordinates," *IEEE Trans. Nucl. Sci.* **30**, 4589–4591 (1983).
123. S. D. Gedney, "An anisotropic perfectly matched layer-absorbing medium for the truncation of FDTD lattices," *IEEE Trans. Antennas Propag.* **44**, 1630–1639 (1996).
124. C. Oh and M. J. Escuti, "Numerical analysis of polarization gratings using the finite-difference time-domain method," *Phys. Rev. A* **76**, 043815 (2007).
125. M. N. Miskiewicz, P. T. Bowen, and M. J. Escuti, "Efficient 3D FDTD analysis of arbitrary birefringent and dichroic media with obliquely incident sources," *Proc. SPIE* **8255**, 82550W (2012).
126. S.-D. Wu and E. N. Glytsis, "Volume holographic grating couplers: rigorous analysis by use of the finite-difference frequency-domain method," *Appl. Opt.* **43**, 1009–1023 (2004).
127. W. Sun, K. Liu, and C. A. Balanis, "Analysis of singly and doubly periodic absorbers by frequency-domain finite-difference method," *IEEE Trans. Antennas Propag.* **44**, 798–805 (1996).
128. R. C. Rumpf, "Simple implementation of arbitrarily shaped total-field/scattered-field regions in finite-difference frequency-domain," *Prog. Electromagn. Res. B* **36**, 221–248 (2012).
129. J.-M. Jin, *The Finite Element Method in Electromagnetics* (Wiley, 2015).
130. M. G. Moharam and T. K. Gaylord, "Rigorous coupled-wave analysis of planar-grating diffraction," *J. Opt. Soc. Am.* **71**, 811–818 (1981).
131. M. G. Moharam, T. K. Gaylord, D. A. Pommet, and E. B. Grann, "Stable implementation of the rigorous coupled-wave analysis for surface-relief gratings: enhanced transmittance matrix approach," *J. Opt. Soc. Am. A* **12**, 1077–1086 (1995).
132. M. G. Moharam and T. K. Gaylord, "Diffraction analysis of dielectric surface-relief gratings," *J. Opt. Soc. Am.* **72**, 1385–1392 (1982).
133. N. Chateau and J.-P. Hugonin, "Algorithm for the rigorous coupled-wave analysis of grating diffraction," *J. Opt. Soc. Am. A* **11**, 1321–1331 (1994).
134. M. G. Moharam and T. K. Gaylord, "Rigorous coupled-wave analysis of grating diffraction—E-mode polarization and losses," *J. Opt. Soc. Am.* **73**, 451–455 (1983).
135. M. G. Moharam and T. K. Gaylord, "Rigorous coupled-wave analysis of metallic surface-relief gratings," *J. Opt. Soc. Am.* **3**, 1780–1787 (1986).
136. E. N. Glytsis and T. K. Gaylord, "Rigorous three-dimensional coupled-wave diffraction analysis of single and cascaded anisotropic gratings," *J. Opt. Soc. Am. A* **4**, 2061–2080 (1987).
137. E. N. Glytsis and T. K. Gaylord, "Three-dimensional (vector) rigorous coupled-wave analysis of anisotropic grating diffraction," *J. Opt. Soc. Am. A* **7**, 1399–1420 (1990).
138. S. Boonruang, A. Greenwell, and M. G. Moharam, "Multiline two-dimensional guided-mode resonant filters," *Appl. Opt.* **45**, 5740–5747 (2006).
139. M. G. Moharam, "Coupled-wave analysis of two-dimensional dielectric gratings," *Proc. SPIE* **883**, 8–12 (1988).
140. S. S. Wang, M. G. Moharam, R. Magnusson, and J. S. Bagby, "Guided-mode resonances in planar dielectric-layer diffraction gratings," *J. Opt. Soc. Am. A* **7**, 1470–1474 (1990).
141. J. Francés, S. Bleda, M. L. Álvarez López, F. J. Martínez Guardiola, A. Márquez, C. Neipp, and A. Beléndez, "Analysis of periodic anisotropic media by means of split-field FDTD method and GPU computing," *Proc. SPIE* **8498**, 84980K (2012).
142. X. Xiang and M. J. Escuti, "Numerical modeling of polarization gratings by rigorous coupled wave analysis," *Proc. SPIE* **9769**, 976918 (2016).
143. X. Xiang and M. J. Escuti, "Numerical analysis of Bragg regime polarization gratings by rigorous coupled-wave analysis," *Proc. SPIE* **10127**, 101270D (2017).